



# Multi-scale modelling of heterogeneous shell structures

T.J. Massart, B.C.N. Mercatoris, Benoît Piezel, P. Berke, Lucien  
Laiarinandrasana, Alain Thionnet

## ► To cite this version:

T.J. Massart, B.C.N. Mercatoris, Benoît Piezel, P. Berke, Lucien Laiarinandrasana, et al.. Multi-scale modelling of heterogeneous shell structures. Computer Assisted Mechanics and Engineering Sciences, 2011, 18, pp.53-71. hal-00714256

**HAL Id: hal-00714256**

**<https://minesparis-psl.hal.science/hal-00714256>**

Submitted on 4 Jul 2012

**HAL** is a multi-disciplinary open access archive for the deposit and dissemination of scientific research documents, whether they are published or not. The documents may come from teaching and research institutions in France or abroad, or from public or private research centers.

L'archive ouverte pluridisciplinaire **HAL**, est destinée au dépôt et à la diffusion de documents scientifiques de niveau recherche, publiés ou non, émanant des établissements d'enseignement et de recherche français ou étrangers, des laboratoires publics ou privés.

# Multi-scale modelling of heterogeneous shell structures

T.J. Massart, B.C.N. Mercatoris, B. Piezel, P. Berke

*Building, Architecture & Town Planning CP 194/2*

*Université Libre de Bruxelles (ULB)*

*Avenue F.D. Roosevelt 50, 1050 Brussels, Belgium*

*e-mail: thmassar@batir.ulb.ac.be*

L. Laiarinandrasana<sup>1</sup>, A. Thionnet<sup>1,2</sup>

<sup>1</sup> *Centre des Matériaux – Mines ParisTech*

*CNRS UMR 7633, BP 87 – 91003 Evry Cedex, France*

<sup>2</sup> *Université de Bourgogne, Mirande*

*BP 47870, 21078 Dijon, France*

This paper reviews multi-scale computational homogenisation frameworks for the non-linear behaviour of heterogeneous thin planar shells. Based on a review of some of the currently available methods, a computational homogenisation scheme for shells is applied on to representative volume elements for plain weave composites. The effect of flexural loading on the potential failure modes of such materials is analysed, focusing on the reinforcement-matrix delamination mechanism. The attention is next shifted toward failure localisation in masonry unit cells. Subsequently, a recently developed computational FE<sup>2</sup> solution scheme accounting for damage localisation at structural scales based on RVE computations is applied.

**Keywords:** thin planar shells, computational homogenisation, failure, textile reinforced composites, masonry.

## 1. INTRODUCTION

The non-linear and failure behaviour of heterogeneous materials is complex to represent computationally due to the presence of numerous competing failure mechanisms, and the difficulty to formulate and identify constitutive laws able to incorporate them. Focusing the interest on mechanical processes only, many examples of such situations can, for instance, be found in textile fabric [36] or woven reinforced composites [23, 42], in which delamination between the reinforcement and the matrix interacts with matrix cracking and delamination between plies. Such mechanisms may be particularly active upon impact or when thin composite structures are loaded perpendicular to their surface. The same type of complex situation is encountered in masonry structures when cracking enters the picture, with potential damage localisation with evolving anisotropic properties of the overall behaviour.

As a complement to closed-form constitutive approaches, multi-scale approaches developed nowadays offer an alternative solution in the characterisation of periodic heterogeneous materials. Different multi-scale techniques have been developed in the past decades allowing postulating closed-form constitutive laws at the scale of the constituents, on which the material parameters are a priori more straightforward to identify. Substructuring methods based on a structural decomposition in non-overlapping subdomains have been proposed for heterogeneous materials, see for instance [11, 21], in which compatibility conditions are used to connect the discretisation of the subdomains to the macroscopic finite element mesh playing the role of a frame. Asymptotic homogenisation was ini-

tially presented for periodic heterogeneous materials in [7, 41], using an asymptotic expansion of the macroscopic variables which allows defining a boundary value problem on a representative volume element (RVE) for each order under consideration, see [37]. This technique is still widely used for composite materials [1, 2, 24]. Based on the scale separation assumption, computational approaches known as  $FE^2$  methods became popular over the last decade. They consist in computing numerically the average non-linear response of a heterogeneous microstructure by means of averaging theorems and a boundary value problem on a RVE [18, 25, 40]. These approaches were later extended to account for structural scale localisation of degradation, either based on gradient enhancements in the scale transitions [26] or on microstructure-informed embedded discontinuities or cohesive zones used at the structural scale [31, 33, 44]. Another multi-scale approach recently proposed uses X-FEM, and consists in feeding the behaviour of structural scale equivalent displacement discontinuities with information extracted from the aggregation of all microstructural material instabilities present in a unit cell, see [5, 6].

Most of these efforts related to multi-scale modelling techniques were devoted until now to 2D or 3D 'classical' representations, assuming periodic boundary conditions on all the faces of 3D RVEs. However, complex heterogeneous materials may appear in shell-like structures such as laminated or textile reinforced composites [22], truss core sandwich components [17, 45], or out-of-plane loaded masonry structures [13]. To account properly for the shell kinematics, the periodicity constraints need to be relaxed on the top and bottom sides of a through-thickness RVE, and average curvatures have to enter the scale transition relations. Extensions of multi-scale computational approaches to shell-like formulations were therefore recently proposed. Unit cell asymptotic homogenisation techniques were used to determine the elastic properties of beam-like structures in [12], of composite shell structures with orthotropic reinforcements in [14], and of periodic running bond masonry walls subjected to out-of-plane loading in [13]. The computational homogenisation strategy was recently extended for structured thin sheets using the homogenisation of a through-thickness RVE based on a second-order strategy [15, 20]. A more restricted periodic homogenisation procedure was presented in [35] for the case of elastic Kirchhoff-Love masonry shells, later explored in [32] and [34] for masonry structures.

In the present contribution, computational homogenisation will be reviewed. RVE computations will be performed for two types of materials. First, the effect of flexural loading will be scrutinised for plain weave composites. Second, localisation under bending in masonry will be analysed. The paper is structured as follows. Section 2 briefly recalls the essentials of homogenisation relations for 3D through-thickness RVEs towards shell formulations. RVE computations are next presented in Sec. 3 for plain weave composites, showing how flexural effects impact potential failure mechanisms in such microstructures. The attention is next focused on localisation detection in the average flexural response of masonry in Sec. 4, illustrating the condition under which meaningful failure indicators can be extracted from the homogenised shell response. In particular, the need to properly generalise the acoustic tensor criterion classically used in 2D or 3D applications is illustrated. The corresponding failure indicators are casted in the frame of a  $FE^2$  computational scheme in Sec. 5 for the direction dependent flexural behaviour of masonry wallets. Finally, Sec. 6 summarises the results and gives future perspectives.

## 2. COMPUTATIONAL HOMOGENISATION FOR THIN SHELLS

The mesostructural material behaviour of constituents is up-scaled computationally towards the membrane-flexural constitutive response by means of a computational homogenisation scheme. The principles of these up-scaling relations were developed in [35] for the elastic membrane-flexural behaviour of thin planar masonry shells and used in [32, 34] for the non-linear behaviour of such a composite material, and will be briefly recalled here for clarity. Obtaining the average macroscopic response of a heterogeneous material from its underlying mesostructure and the behaviour of its constituents can be based on the solution of a mesostructural boundary value problem on a rep-

representative volume element (RVE) relying on averaging theorems. A principle of scale separation between the two scales of representation is used, which assumes that the material configuration is macroscopically homogeneous, but microscopically heterogeneous [25]. Here, a three-dimensional through-thickness RVE is used to represent the mesostructure. Considering the classical simplifying assumptions in engineering planar shell descriptions, the scale transitions need to be carefully derived especially for the transverse shear behaviour of thick shells, see [15, 20].

### 2.1. Averaging relations for the Kirchhoff-Love planar shell kinematics

At the fine scale, a planar shell is represented by a prismatic through-thickness RVE, defined by its trace  $\mathcal{S}_{\text{RVE}}$  on the reference surface of the shell and its thickness  $h$ , corresponding to the shell thickness [20]. The averaging theorems linking the coarse (macro) scale and the fine (meso) scale quantities have to be verified for the strain, the stress and the work variations. For the case of the Kirchhoff-Love planar shell kinematics, it is postulated that the macroscopic membrane strain tensor  $\mathbf{E}$  is the average of the local membrane strain tensor over the reference surface  $\mathcal{S}_{\text{RVE}}$ . The macroscopic curvature tensor  $\boldsymbol{\chi}$  is assumed to be the surface average of the local curvature tensor over  $\mathcal{S}_{\text{RVE}}$

$$\mathbf{E} = \frac{1}{\mathcal{S}_{\text{RVE}}} \int_{\mathcal{S}_{\text{RVE}}} (\nabla \mathbf{u}_r)^{\text{sym}} d\mathcal{S}_{\text{RVE}}, \quad (1)$$

$$\boldsymbol{\chi} = \frac{1}{\mathcal{S}_{\text{RVE}}} \int_{\mathcal{S}_{\text{RVE}}} -\nabla \nabla u_z d\mathcal{S}_{\text{RVE}}, \quad (2)$$

where  $\mathbf{u}_r$  and  $u_z$  are the projections of the mesostructural displacement vector, respectively, on the reference surface and in the thickness direction. The energy consistency is classically assumed, and expressed here by

$$\mathbf{N} : \delta \mathbf{E} + \mathbf{M} : \delta \boldsymbol{\chi} = \frac{1}{\mathcal{S}_{\text{RVE}}} \int_{\mathcal{V}_{\text{RVE}}} \boldsymbol{\sigma} : \delta \boldsymbol{\varepsilon} d\mathcal{V}_{\text{RVE}}, \quad (3)$$

where  $\boldsymbol{\varepsilon}$  is the mesostructural infinitesimal strain tensor work conjugate to the mesoscopic stress field  $\boldsymbol{\sigma}$ , and  $\mathbf{N}$  and  $\mathbf{M}$  are respectively the macroscopic membrane force and bending moment tensors. Combining (1), (2) and (3) with appropriate boundary conditions on the RVE leads to the satisfaction of the averaging theorem for the stress measures and allows relating the macroscopic membrane force tensor  $\mathbf{N}$  and the macroscopic bending moment tensor  $\mathbf{M}$  to the mesoscopic statically admissible stress field  $\boldsymbol{\sigma}$  at the surface of the RVE.

### 2.2. Homogenisation with periodic boundary conditions

Here, the coupled two-scale framework will be defined assuming periodicity of the mesostructure, and will be illustrated for the particular case of a textured material such as a three-dimensional composite. Periodic boundary conditions on RVEs were shown to provide a better estimation of the overall elastic properties than other boundary conditions, see [25, 40]. Suppressing the rigid body translations and rotations of the RVE, the kinematically admissible displacement field is strain-periodic and given by [35]

$$\mathbf{u}_r = \mathbf{E} \cdot \mathbf{x}_r + z \boldsymbol{\chi} \cdot \mathbf{x}_r + \mathbf{u}_r^p, \quad (4)$$

$$u_z = -\frac{1}{2} \mathbf{x}_r \cdot \boldsymbol{\chi} \cdot \mathbf{x}_r + u_z^p, \quad (5)$$

where  $\mathbf{u}_r^p$  and  $u_z^p$  are in-plane and out-of-plane periodic displacement fluctuation fields, added to the average displacement field to account for the heterogeneity of the material. For such a displacement field, the averaging relations (1) and (2) are satisfied, and both fluctuation fields can be eliminated. The periodic boundary conditions can be prescribed on the RVE using tying relations between boundary points related by periodicity, which are expressed in the sequel and in [35].

### 2.3. Control system of the mesoscopic boundary value problem

The proper size and geometry of a RVE should be deduced from statistical considerations [46], or defined by the periodicity of a given mesostructure. In the case of a small strain description, the Kirchhoff-Love generalised strains are given by six independent scalar quantities. The average deformed state of a RVE can therefore be fully prescribed using six displacements if periodicity is enforced. A possible choice for these six controlling displacements is given in Fig. 1, for the case of woven composites in which the periodic structure allows the use of perpendicular planar boundaries of a 3D through-thickness RVE.

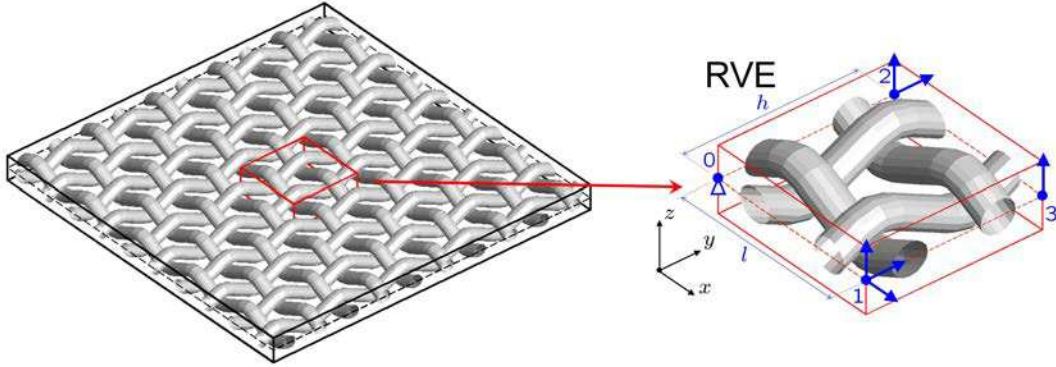


Fig. 1. Control displacements system for a plain weave composite RVE.

The macroscopic membrane deformations are prescribed using three reference plane displacements, while the macroscopic curvatures are fixed by three out-of-plane displacements. Using Eqs. (1), (2), (4) and (5) as well as the periodicity conditions, the relations linking the controlling displacements to the average coarse-scale strains can be written as:

$$u_1^1 = lE_{11}, \quad (6a)$$

$$u_2^1 = lE_{12}, \quad (6b)$$

$$u_2^2 = hE_{22}, \quad (6c)$$

$$u_3^1 = -\frac{l^2}{2}\chi_{11}, \quad (6d)$$

$$u_3^2 = -\frac{h^2}{2}\chi_{22}, \quad (6e)$$

$$u_3^3 = -\frac{l^2}{2}\chi_{11} - hl\chi_{12} - \frac{h^2}{2}\chi_{22}. \quad (6f)$$

These relations can be recast in a matrix form reading:

$$\{u_{ctl}\} = [D_u]^{-1}\{E_{KL}\}, \quad (7)$$

where  $\{u_{ctl}\}$  is a column vector of the six controlling degrees of freedom,  $\{E_{KL}\}$  is a column vector of the Kirchhoff-Love generalised strains, and  $[D_u]$  is a matrix which depends on the in-plane dimensions of the RVE. Similarly, considering (3), (4) and (5), the average Kirchhoff-Love

stresses can be obtained from the controlling forces conjugated to the controlling displacements, and which represent the action of the neighbouring cells, see [32] for the detailed development. For the considered unit cell, these relations read:

$$N_{11} = \frac{1}{h} f_1^1, \quad (8a)$$

$$N_{22} = \frac{1}{l} f_2^2, \quad (8b)$$

$$N_{12} = \frac{1}{2h} f_2^1, \quad (8c)$$

$$M_{11} = -\frac{l}{2h} f_3^1 - \frac{l}{2h} f_3^3, \quad (8d)$$

$$M_{22} = -\frac{h}{2l} f_3^2 - \frac{h}{2l} f_3^3, \quad (8e)$$

$$M_{12} = -\frac{1}{2} f_3^3. \quad (8f)$$

In a matrix form, this can be written as:

$$\{\Sigma_{KL}\} = [D_f] \{f_{ctl}\}, \quad (9)$$

where  $\{f_{ctl}\}$  is a column vector of the six controlling forces,  $\{\Sigma_{KL}\}$  is a column vector of the Kirchhoff-Love generalised stresses, and  $[D_f]$  is a matrix which depends on the in-plane dimensions of the RVE. Upon solving the RVE equilibrium boundary value problem for a given macroscopic generalised strain using a computational approach (finite element method), a mesostructural tangent stiffness  $[K]$  is readily available, linking variations of forces and displacements. This discretised tangent stiffness relation of the RVE can be condensed on the controlling displacements, yielding  $\{\delta f_{ctl}\} = [K^*] \{\delta u_{ctl}\}$  where  $[K^*]$  is the fine-scale (discrete) tangent stiffness matrix condensed at the controlling degrees of freedom. Combining this condensed mesostructural tangent relation with variations of (7) and (9) allows identifying the matrix relating variations of the generalised stresses  $\{\delta \Sigma_{KL}\}$  to those of the generalised strains  $\{\delta E_{KL}\}$  as:

$$[L] = [D_f][K^*][D_u]^{-1}, \quad (10)$$

where  $[L]$  is nothing else than the matrix form of the homogenised membrane-flexural material tangent stiffness defined as [32]

$$\begin{aligned} \delta \mathbf{N} &= {}^4 \mathbf{L}_{mm} : \delta \mathbf{E} + {}^4 \mathbf{L}_{mf} : \delta \boldsymbol{\chi}, \\ \delta \mathbf{M} &= {}^4 \mathbf{L}_{fm} : \delta \mathbf{E} + {}^4 \mathbf{L}_{ff} : \delta \boldsymbol{\chi}. \end{aligned} \quad (11)$$

Note once again that these relations identifying the coarse-scale (macroscopic) material tangent stiffness are obtained computationally. The details of the fine-scale constitutive laws are implicitly accounted for in the condensed mesostructural tangent stiffness  $[K^*]$ , and no closed-form relation between the fine-scale constitutive description and the tangents in (11) is required or available.

Based on Eq. (7), any average generalised deformation path can be prescribed. The related mesostructural boundary value problem is completely defined from the prescribed controlling degrees of freedom and the periodicity boundary conditions, and can be solved using a classical finite element scheme, provided mesostructural constitutive laws are postulated. This type of control is classically used in multi-scale nested scheme using displacement-based finite element schemes, [25, 30].



### 3. PLAIN WEAVE COMPOSITES RVE COMPUTATIONS

#### 3.1. Study of plain weave composites unit cell

The previous homogenisation framework is now applied to a plain weave composite unit cell which consists in a single period RVE. The considered matrix is a polyvinyl chloride (PVC) matrix with a thickness of 4 mm. The textile is composed of polyethylene terephthalate (PET) fibres for the warp yarns and polyamide 6-6 (PA66) fibres for the weft yarns. The repeating pattern is therefore the simplest possible, and is represented in Fig. 2. Because of the complexity of the fabric pattern, the meshing tools developed in [28, 43] have been used. Conditions of periodicity are imposed on the different faces of the cell in order to allow imposing the conditions (4) and (5). The meshing obtained is then transferred toward ZeBuLoN FE code [9] developed by MINES ParisTech. Computations are carried out with the ZeBuLoN code.

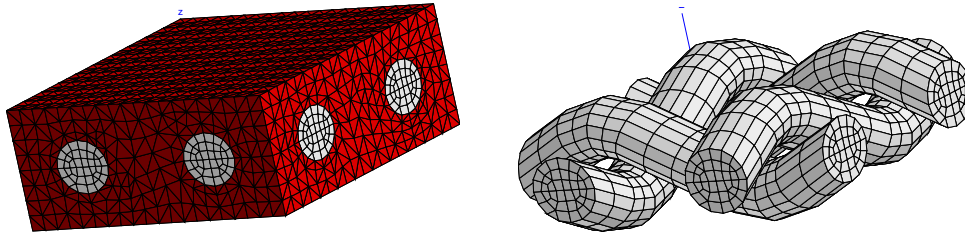


**Fig. 2.** Discretised periodic RVE for a plain weave composite (left) full RVE mesh with (right) reinforcement discretisation. The unit cell consists of a single period RVE.

At the macroscopic scale, due to the symmetries of its microstructure, the composite can be considered initially orthotropic. The mesoscopic scale allows taking the geometry of the fabric into account. The focus here will be set on assessing the impact of changes at the mesoscopic scale on the resulting macroscopic scale. While some contributions assess the out-of-plane loading of plain weave textiles themselves [36], most of the recently available contributions related to the multi-scale analysis of complex textile reinforced composites, are focused on the in-plane response of the material with periodic homogenisation [1] to extract average material properties. Recently, the local damage evolution under static tension for satin weave composites was analysed in [16]. The case of laminates made of several plain weave layers subjected to in-plane tension was recently investigated in [22]. Specific boundary conditions on the RVE were defined to be applied on single layer RVEs to distinguish between the response of inner and outer layers, and avoiding periodic boundary conditions along the thickness. In the present contribution, a complementary approach is used where through-thickness RVEs will be used to allow assessing flexural loading effects.

#### 3.2. Mesoscopic constitutive setting

The behaviour of the components (yarns and matrix) was reported elsewhere [38, 39]. The following simplifying assumptions are used. The behaviour of the matrix is assumed isotropic. The variations of longitudinal yarns properties induced by their own strain are neglected [4, 19]. The non-linear behaviour of the yarns can be identified by tensile tests as shown in [38, 39]. Three different domains can be identified, namely an elastic domain, before a stiffening of the yarns, followed by the reduction of the tangent modulus and finally failure. These two last effects are not incorporated here. The increase of stiffness observed during the monotonous tensile tests was modelled with an elastoplastic behaviour with two isotropic hardenings [8, 27]. The deformation is partitioned according to:

$$\boldsymbol{\epsilon} = \boldsymbol{\epsilon}_e + \boldsymbol{\epsilon}_p, \quad (12)$$

with  $\underline{\epsilon}_e$  – the elastic part of the total strain and  $\underline{\epsilon}_p$  – the plastic strain. The adopted yield function reads

$$f(\underline{\sigma}, R) = J(\underline{\sigma}) - R, \quad (13)$$

where  $J$  is the second invariant of the stress deviator defined by the equation:

$$J = \left( \frac{3}{2} s_{ij} s_{ij} \right)^{1/2}, \quad (14)$$

with  $\underline{s}$  the stress deviator.  $R$  is a scalar variable defining the isotropic hardening behaviour of the material. Its evolution laws reads:

$$R = R_0 + Q(1 - e^{-bp}) + A(e^{Bp} - 1), \quad (15)$$

with  $p$  – the cumulated plastic strain, and  $R_0$ ,  $Q$ ,  $b$ ,  $A$  and  $B$  material parameters to be determined. The increase of tangent modulus of the yarns with plastic strain is incorporated by the second isotropic hardening terms of Eq. (15). The five parameters can be obtained by inverse methods from the results of tensile tests carried out on the composite material as explained in [38]. The same parameters as in [38] are used for the sequel of this section and are reported in Table 1. Note that the behaviour of the reinforcing material is approximated with an isotropic law. This might induce an overestimation of the transverse stiffness in the results.

**Table 1.** Material parameters for plain weave composite RVE computations:  
(a) matrix, (b) warp yarns, (c) weft yarns.

	$E$ [MPa]	$\nu$	$R_0$ [MPa]	$Q$ [MPa]	$b$	$A$ [MPa]	$B$
(a)	400	0.3	–	–	–	–	–
(b)	15000	0.3	59	63	363	5.45	53.4
(c)	2996	0.3	5.6	15.34	403	7.4	68.9

### 3.3. Delamination stresses under flexural loading

Based on relations (6) and (8), the average response of the composite shell can be deduced for any strain or stress path. The effect of flexural loading on the potential delamination failure mechanism of textile reinforced composites will here be assessed assuming that the composite shell is used in a conveyor belt type application, see Fig. 3. To fix the imposed average deformations of the RVEs with realistic values, the composite shell will be subjected to an in-plane tension corresponding to the pre-tension present in a conveyor belt. In addition to this in-plane tension, the conveyor belt is subjected to bending when passing on conveyor pulleys. Here, it is assumed that the pre-tension applied to such a conveyor belt is such that average longitudinal strain reaches a value of  $E_{LL} = 0.0018$ . For the flexural effect, it is assumed that the belt is bent around the conveyor pulley with a radius of 200 mm, which sets the imposed curvature on the RVE given its thickness. The RVE computations presented below match these two imposed macroscopic strains. In the sequel, the case of a single plane weave unit cell is first considered, followed by the case of a stacking of four plane weave reinforced plies, as illustrated in Fig. 3.

First an in-plane tension along the direction of the yarns is considered, in which the shell homogenisation is used. Second, a combined tension-bending case is considered with the shell flexural homogenisation scheme to assess the potential influence of bending on delamination. For both cases, the focus is set on the stress state at the interface between the reinforcement and the matrix in order to assess the risk for delamination between both constituents. In order to compare the different stress states at the interfaces between the reinforcement and the matrix, a simplified local stress criterion is adopted to assess potential delamination, defined as:

$$\sigma_{delamination} = \sqrt{\sigma_{nn}^2 + \alpha \tau_{eq}^2} \leq \sigma_{max, interface}, \quad (16)$$



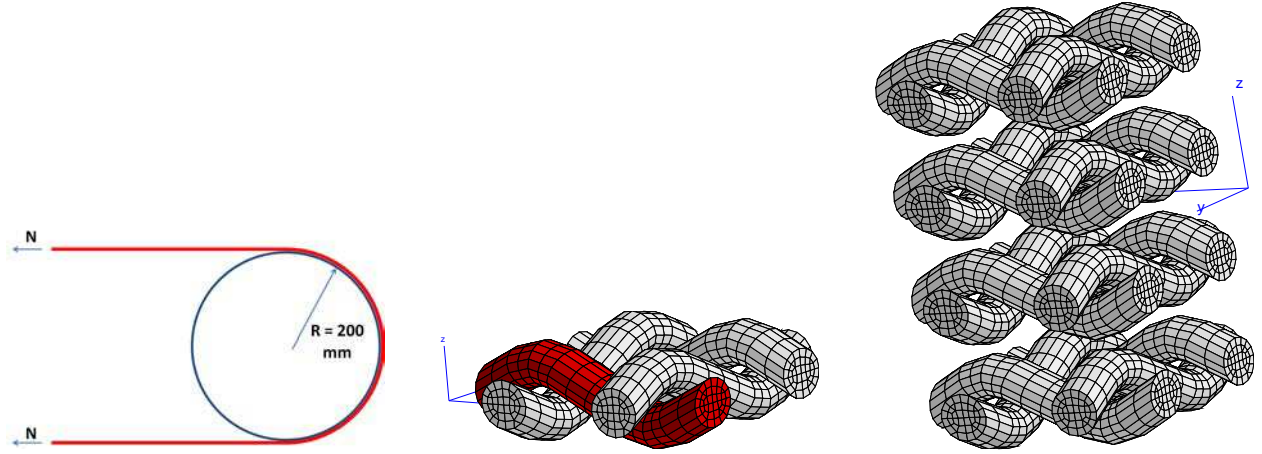


**Fig. 3.** Plain weave reinforced composites unit cells investigated: (left) loading scheme, (center) single layer RVE (the highlighted warp yarn will be the depicted in the stress maps), (right) RVE for stacking of four plain weave plies.

where  $\sigma_{nn}$  is the stress component normal to the interface (peeling stress),  $\tau_{eq} = \sqrt{\tau_{nt}^2 + \tau_{ns}^2}$  is the tangential projection of the stress vector at the interface, and  $\alpha$  is a coefficient accounting for the relative contribution to failure of the interface of mode-I and mode-II stress components. Note that only the distribution of the quantity defined by relation (16) will be analysed here, without explicitly modelling the progressive degradation of the interface properties.

**In-plane tension.** As a first illustration, the results obtained for in-plane tension loading obtained by the homogenisation are reported on Fig. 4. Figure 4 depicts the contributions of each stress component present in (16) for the yarns in the warp direction (a single yarn is plotted to ease interpretation due to the symmetry of the two warp yarns in the cell). Under this pure tension case, the peeling stress  $\sigma_{nn}$  remains limited to 2.1 MPa. The delamination stress simplified criterion (16) reaches a value of 2.5 MPa. Clearly, such stress levels at the interface between the yarns and the matrix are not suggesting potential delamination problems.

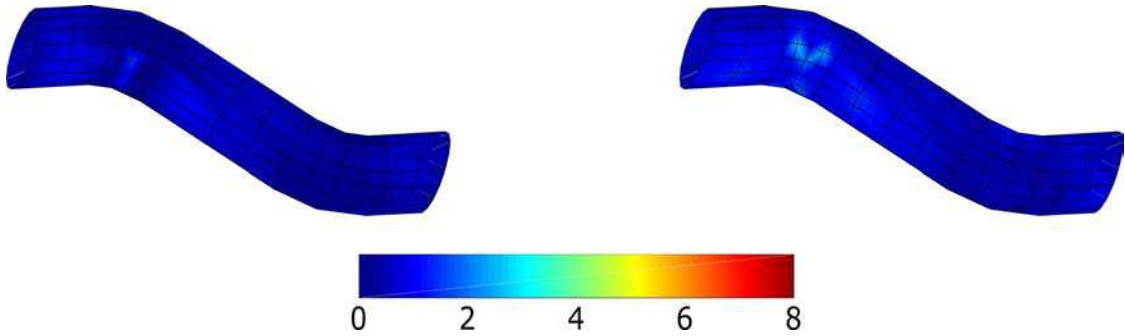


**Fig. 4.** Stress state at the warp yarns – matrix interface for in-plane tension along the warp direction: (left) normal (peeling) stress  $\sigma_{nn}$ , (right) delamination stress defined by (16) with  $\alpha = 0.5$ . The colorbar is adapted to ease the comparison with Fig. 5.

**Tension-bending.** Bending is next added to tension, assuming proportional loading for the sake of simplicity. A curvature is added with the value  $\chi = \frac{1}{R}$  with  $R$  the radius of the conveyor pulley over which the belt is bent. Figure 5 depicts the various stress components entering relation (16). Due to the flexural effect captured by the shell scale transitions, the peeling stress  $\sigma_{nn}$  now reaches a maximal value of 6 MPa, while the tangential component reaches 8 MPa. The delamination stress criterion (16) is now increased up to 8 MPa. These stress levels suggest that the incorporation of the flexural effect may, indeed, play a crucial role in a delamination process in such a conveyor belt.

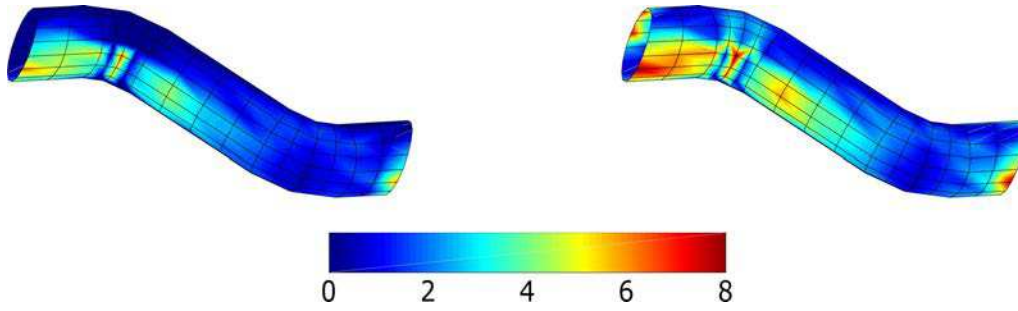


**Fig. 5.** Stress state at the warp yarns – matrix interface for in-plane tension along the warp direction combined with bending: (left) normal (peeling) stress  $\sigma_{nn}$ , (right) delamination stress defined by (16) with  $\alpha = 0.5$ .

**Stacked plain weave plies.** Finally, the same tension-bending simulations are performed for a unit cell made of four stacked plain weave plies. Since the thickness of the shell increases, the bending component will generate higher strains in the outer layers of the shell when passing on to the conveyor pulley. For the same loading conditions (same in-plane deformation and same curvature matching a conveyor pulley with a 200 mm radius), Fig. 6 depicts the stress state at the interface between the warp yarns and the matrix for the outer ply. The peeling and the delamination stresses are as high as 30 MPa in this case, which clearly suggests that delamination should be a concern.

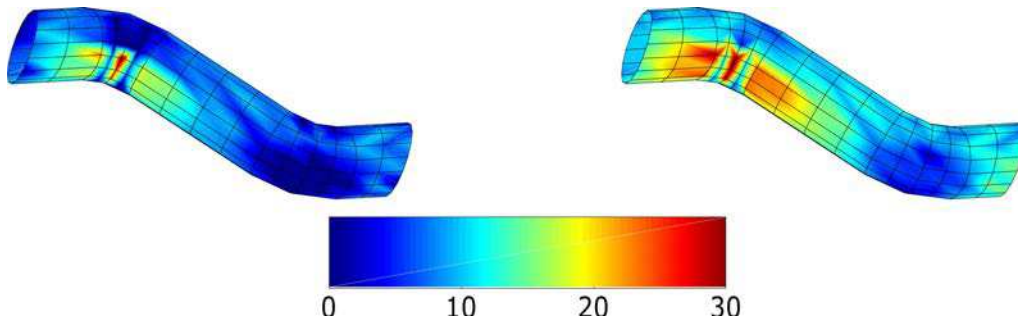


**Fig. 6.** Unit cell composed of four plain weave plies – Stress state at the warp yarns – matrix interface for in-plane tension along the warp direction combined with bending: (left) normal (peeling) stress  $\sigma_{nn}$ , (right) delamination stress defined by (16) with  $\alpha = 0.5$ .

## 4. LOCALISATION OF DAMAGE IN MASONRY SHELLS

### 4.1. Non-orthogonal periodic boundary conditions

As shown in [32, 35], the scale transition relationships (6) and (8) can be modified to account for non orthogonal RVE boundaries, as for the specific stacking of constituents in masonry material, see Fig. 7. In such a case, relations (6) and (8) are modified to account for the periodicity parameters  $l$ ,  $h$  and  $d$  as defined in [32]. The definitions of matrices in (7) and (9) are updated accordingly.

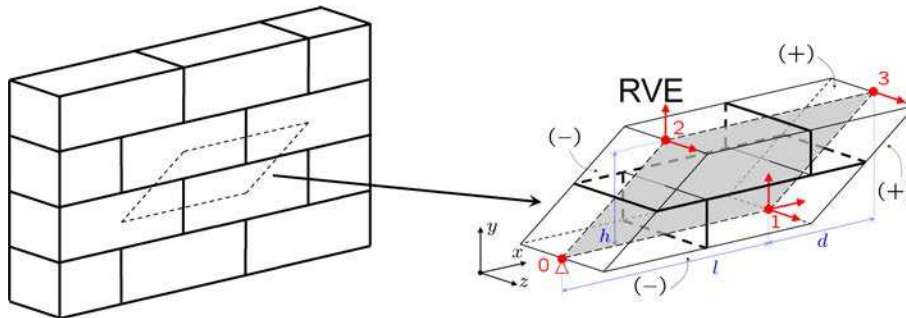


**Fig. 7.** Through-thickness RVE for running bond masonry [35].

## 4.2. Extraction of average localisation orientations

For the appearance of localisation at the structural scale, a criterion to detect localisation and its orientation in shells is required, which should be based on the computational response of mesostructural RVEs. Assuming a thin shell behaviour (no transverse shear effects) and an initially planar structure, a criterion proposed in [29] is used, which was shown in [32] to properly detect localisation in the context of two-scale computations. The procedure is based on the homogenised material tangent stiffness governing the constitutive response (11), which can be deduced from the stiffness of the RVE condensed at the controlling degrees of freedom by relation (10). The conditions for the appearance of localisation in which material degradation occurs can be detected as a material bifurcation. Across the interface between such a localising zone ( $l$ ) and its surrounding material ( $s$ ), the displacement and rotation fields can be assumed to be continuous and the generalised strain jumps have the form:

$$\begin{aligned}\delta\mathbf{E}^{(l)} - \delta\mathbf{E}^{(s)} &= \frac{1}{2} (\delta\mathbf{m}_E \mathbf{n} + \mathbf{n} \delta\mathbf{m}_E), \\ \delta\boldsymbol{\chi}^{(l)} - \delta\boldsymbol{\chi}^{(s)} &= \frac{1}{2} (\delta\mathbf{m}_\chi \mathbf{n} + \mathbf{n} \delta\mathbf{m}_\chi),\end{aligned}\tag{17}$$

where  $\mathbf{n}$  is the normal to the localising zone, and  $\mathbf{m}_E$  and  $\mathbf{m}_\chi$  are strain jumps, which vanish in the initial, homogeneous situation. These jumps must become nonzero for a localised state to exist. Using equilibrium, i.e., the continuity of the projected stress quantities at the interface of the localising zone:

$$\begin{aligned}\mathbf{n} \cdot (\delta\mathbf{N}^{(l)} - \delta\mathbf{N}^{(s)}) &= 0, \\ \mathbf{n} \cdot (\delta\mathbf{M}^{(l)} - \delta\mathbf{M}^{(s)}) &= 0\end{aligned}\tag{18}$$

and by introducing Eqs. (11) and (17) in (18) with the classical linear comparison solid assumption (same material stiffness tangents on both sides of the localising zone interface), the stress continuity requirement reads:

$$\begin{bmatrix} (\mathbf{n} \cdot {}^4\mathbf{L}_{mm} \cdot \mathbf{n}) & (\mathbf{n} \cdot {}^4\mathbf{L}_{mf} \cdot \mathbf{n}) \\ (\mathbf{n} \cdot {}^4\mathbf{L}_{fm} \cdot \mathbf{n}) & (\mathbf{n} \cdot {}^4\mathbf{L}_{ff} \cdot \mathbf{n}) \end{bmatrix} \begin{Bmatrix} \mathbf{m}_E \\ \mathbf{m}_\chi \end{Bmatrix} = 0.\tag{19}$$

This system of equations admits a non-trivial solution if

$$\det(\mathbf{A}(\mathbf{n})) = \det \left( \begin{bmatrix} (\mathbf{n} \cdot {}^4\mathbf{L}_{mm} \cdot \mathbf{n}) & (\mathbf{n} \cdot {}^4\mathbf{L}_{mf} \cdot \mathbf{n}) \\ (\mathbf{n} \cdot {}^4\mathbf{L}_{fm} \cdot \mathbf{n}) & (\mathbf{n} \cdot {}^4\mathbf{L}_{ff} \cdot \mathbf{n}) \end{bmatrix} \right) = 0\tag{20}$$

for some direction  $\mathbf{n}$ , where  $\mathbf{A}(\mathbf{n})$  is the acoustic tensor generalised to the Kirchhoff-Love shell theory, see [29, 32]. A negative local maximum of the acoustic tensor determinant spectrum derived from the homogenised material tangent stiffness was shown to match average orientations of coarse-scale localisation consistent with fine-scale damage patterns. This criterion can be used to determine an average localisation orientation in combination with the criterion for the loss of uniqueness of the discretised fine-scale boundary value problem, based on the nonpositive-definite character of its discretised tangent stiffness  $[K^*]$  used to detect the onset of localisation [10]. As will be illustrated in Subsec. 4.4, it is crucial to use the complete generalised acoustic tensor defined in (20) including the membrane flexural couplings to properly detect multi-scale localisation for quasi-brittle materials.

## 4.3. Constitutive setting

A simplified fine-scale constitutive setting for masonry joints is used here (the bricks are assumed to be elastic). The behaviour of joints is modelled by initially elastic planar interface elements, for

which both the normal and tangential stiffnesses ( $k_n, k_t, k_s$ ) can be related to the elastic behaviour of mortar. The tangential stiffnesses are assumed here to be equal ( $k_t = k_s$ ). Depending on the loading mode, either a classical Mohr-Coulomb-type strength criterion or a tension cutoff is used, see Fig. 8. The parameter  $f_t$  is the tensile mode I strength of the mortar or mortar-brick interfaces, while  $c$  is the cohesion and  $\varphi$  is the friction angle of the mortar joints. The compressive behaviour can be considered, defined by a uniaxial compressive strength, and the angle of the compressive cap with respect to the  $\sigma$  axis. A scalar damage model with an exponential evolution law is considered. The traction-separation law, which links the traction vector  $\mathbf{t}$  across the interface to the relative displacement vector  $\boldsymbol{\delta}$ , is given by

$$\mathbf{t} = (1 - D) \mathbf{H} \cdot \boldsymbol{\delta}, \quad (21)$$

where  $D$  is the scalar damage variable growing from zero (virgin material) to one (complete failure) and  $\mathbf{H}$  is a three-dimensional elastic stiffness (second order tensor) which depends on the elastic stiffnesses  $k_n$  and  $k_t$ . The damage evolution law of the mortar joint is given by

$$D(\kappa) = 1 - \frac{f_t}{k_n \kappa} e^{-\frac{f_t}{G_f} \left( \kappa - \frac{f_t}{k_n} \right)} \quad \text{for } \kappa \geq \frac{f_t}{k_n}, \quad (22)$$

where  $G_f$  is the mode I tensile fracture energy. Since the considered interface is three-dimensional and in order to take into account the different behaviours in tension and compression, the damage-driving parameter  $\kappa$  is taken as the most critical value of an equivalent relative displacement defined by

$$\delta_{eq} = \max \left\{ \begin{array}{c} \frac{f_t}{c} \tan \varphi \delta_n + \frac{f_t}{c} \frac{k_t}{k_n} \sqrt{\delta_s^2 + \delta_t^2} \\ \delta_n \\ -\frac{f_t}{f_c} \delta_n + \frac{f_t}{f_c} \frac{k_t}{k_n} \frac{1}{\tan \vartheta} \sqrt{\delta_s^2 + \delta_t^2} \end{array} \right\}. \quad (23)$$

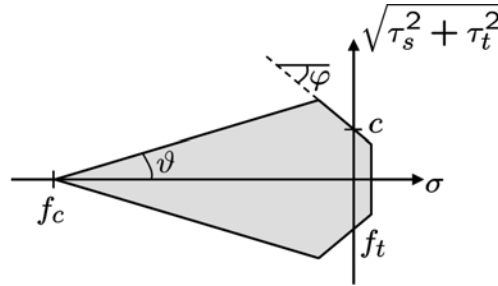


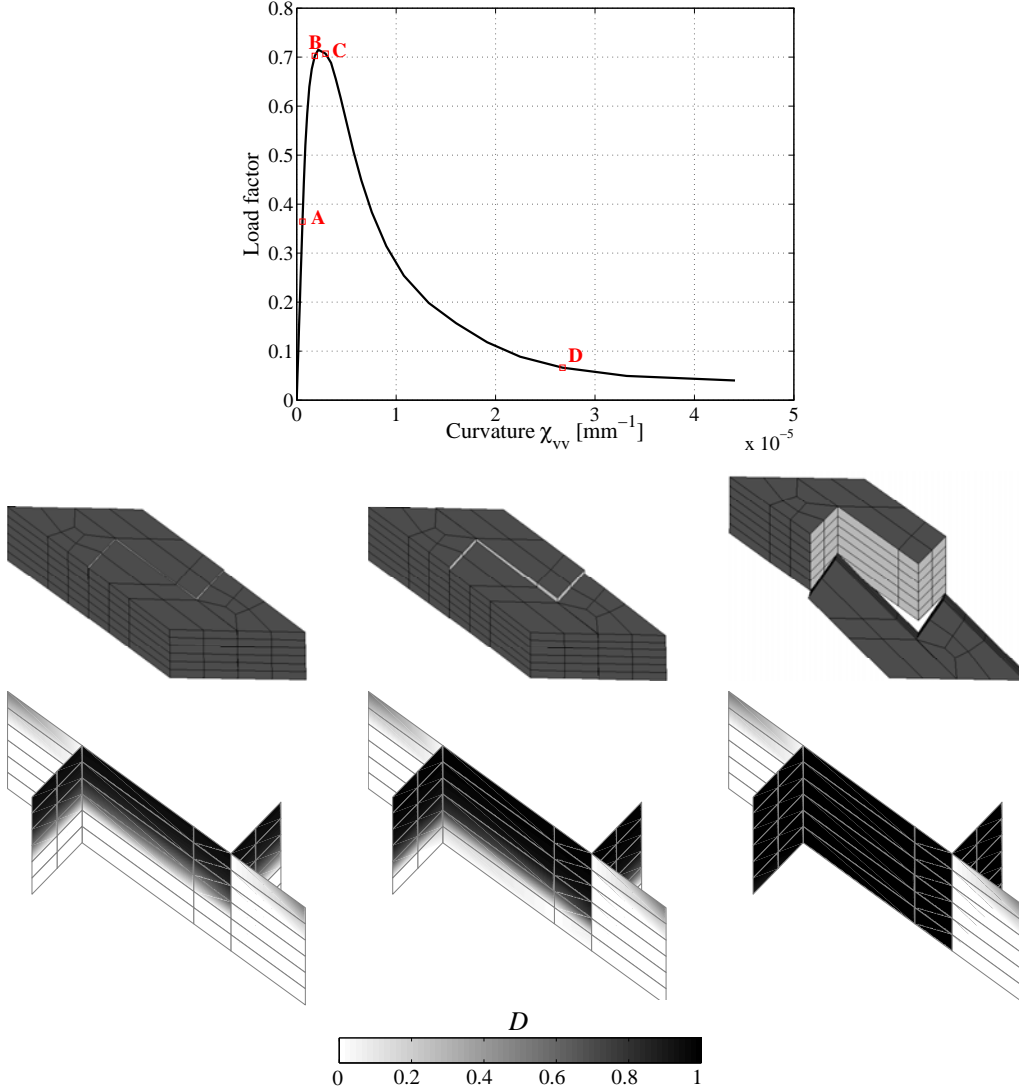
**Fig. 8.** Mohr-Coulomb criterion with tensile cutoff and compressive cap for the mortar joint/mortar-brick interface.

#### 4.4. Localisation analysis for RVE

In this Section, a localisation analysis is performed on a RVE in order to show how meaningful average cracking orientations can be extracted from fine-scale computations. The unit cell represented in Fig. 7 is considered with dimensions  $l = 200$  mm,  $d = 100$  mm,  $h = 80$  mm, and with a thickness of 100 mm. The material parameters used in constituents (bricks and mortar joints) are given in Table 2. The cell is loaded with a bending moment  $M_{vv} = 1500$  kNm/m corresponding to an axis  $v$  at  $50^\circ$  from the vertical direction counterclockwise. This loading is expected to result in a stair-case crack failure mode, the orientation of which can be deduced from geometrical arguments at  $-51.34^\circ$ . The response of the unit cell is depicted in Fig. 9, where the deformed state of

**Table 2.** Material parameters for localisation analysis on a masonry unit cell: (a) Brick and (b) mortar/mortar-brick interface.

	$E$ [MPa]	$\nu$	$k_n$ [MPa/mm]	$k_t$ [MPa/mm]	$f_t$ [MPa]	$G_f$ [mJ/mm <sup>2</sup> ]	$c$ [MPa]	$\varphi$ [°]	$f_c$ [MPa]	$\vartheta$ [°]
(a)	16700	0.15	—	—	—	—	—	—	—	—
(b)	—	—	438	182	0.18	0.005	0.28	36	3.0	45

**Fig. 9.** Global response of the unit cell subjected to bending with stair-case crack opening. The amplified deformed shape and the damage states are illustrated for states B (left), C (center) and D (right) of the response curve.

the cell (with amplification) and the damage state in mortar joints are illustrated. Starting from state B, one can clearly see the stair-case flexural crack initiating as from the peak of the global response of the cell. The localisation orientation detection criterion defined in Subsec. 4.2 is now scrutinised in Figs. 10 and 11. The orientation spectrum of the determinant of the acoustic tensor components is depicted in Fig. 10 for states C and D of the unit cell corresponding to the softening range of the cell global response. It can be noted that the spectrum of the full tensor determinant indeed presents negative values for a range of orientations surrounding the average orientation of the flexural crack (Fig. 10 top). It is emphasized that the partial acoustic tensors based only on the flexural tangent stiffness  $L_{ff}$  and on the membrane tangent stiffness  $L_{mm}$  of the cell do not

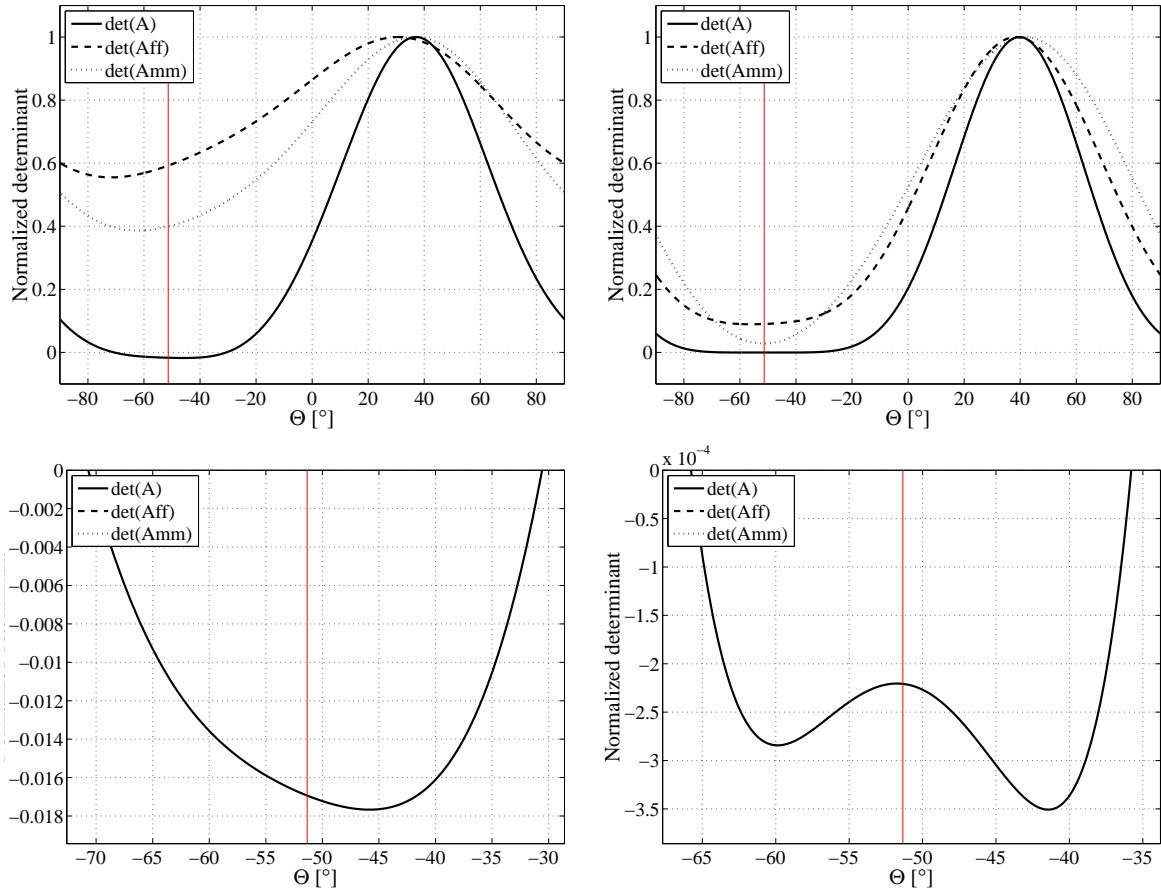


**Fig. 10.** Flexural stair-case failure of a masonry unit cell – orientation spectrum of the acoustic tensor components (flexural part, membrane part, full tensor). (Top) complete spectrum, (bottom) zoom on negative range of the full tensor determinant spectrum. The red vertical line represents the expected localisation orientation based on the geometrical average orientation of the stair-case crack.

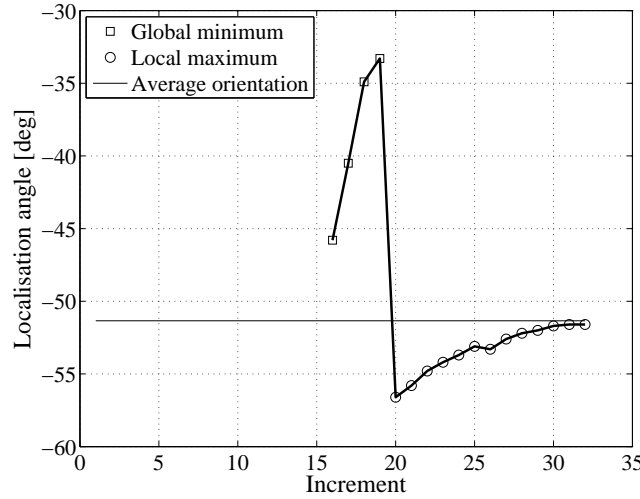


**Fig. 11.** Flexural stair-case failure of a masonry unit cell – evolution of the average crack orientation of the cell towards the geometrically motivated orientation.

satisfy the criterion. Even though a bending loading scheme is applied, membrane-flexural coupling terms appear in the average tangent response of the cell as a result of the different responses of the fine-scale mortar joints for tensile and compressive stress states. Figure 10 shows that neglecting these coupling terms does not allow a proper localisation analysis. Furthermore, the zoom on the



negative values of the full acoustic tensor determinant spectrum (bottom of Fig. 10) indicates that an extremum is found converging towards the expected orientation, as damage progresses through the width of the joint. This confirms that the localisation criterion based on the average acoustic tensor properly characterises the cracking orientation. The convergence of the extremum towards this orientation is illustrated in Fig. 11. As illustrated in Fig. 10, the precise orientation matches a local maximum of the determinant in the negative range. Even though, there is no formal justification to select a precise orientation within the fan of negative values, this example suggests that this extremum should be selected in view of the damage maps presented in Fig. 9.

## 5. UP-SCALING OF FAILURE BEHAVIOUR

### 5.1. Homogenisation towards structural scale cohesive response

Based on the localisation detection presented above, it is possible to extract the information required to treat the global softening response in RVEs. The core ingredients were presented recently in [34] and are as follows. Before localisation, a  $FE^2$  type strategy is used in which the response of the quadrature points of the shell elements is computed as depicted in Fig. 12. At each converged equilibrium configuration, each point of the structure is tested according to the localisation criterion developed above. Based on the result of the localisation analysis, an embedded strong discontinuity is incorporated in the elements for which localisation was detected. This discontinuity introduces jumps in the deflection, the in-plane displacements, and the rotation fields, which are meant to account, in an average sense, for the fine-scale opening of mortar joints. From a finite element interpolation viewpoint, the formulation of such a discontinuity can be based on the developments presented in [3]. In contrast with [3], a closed form expression of the constitutive law governing the behaviour of this discontinuity is here not available, due to the multi-scale nature of the framework. As a result, the behaviour of the softening discontinuity has to be obtained from RVE computations based on the updated scheme illustrated in Fig. 13. For each element in which a discontinuity is inserted, two different unit cells are considered. A first unit cell is used to characterise the response of the bulk of the finite element, which will be assumed in the sequel to unload along a secant stiffness. A second, further damaging, unit cell is used to extract an equivalent traction-opening response of the discontinuity. Since the response of this further damaging unit cell refers to a finite volume of material characterised by a width  $w_n$ , this quantity has to enter the scale transition. The expressions relating the RVE quantities (curvatures, average strains, generalised

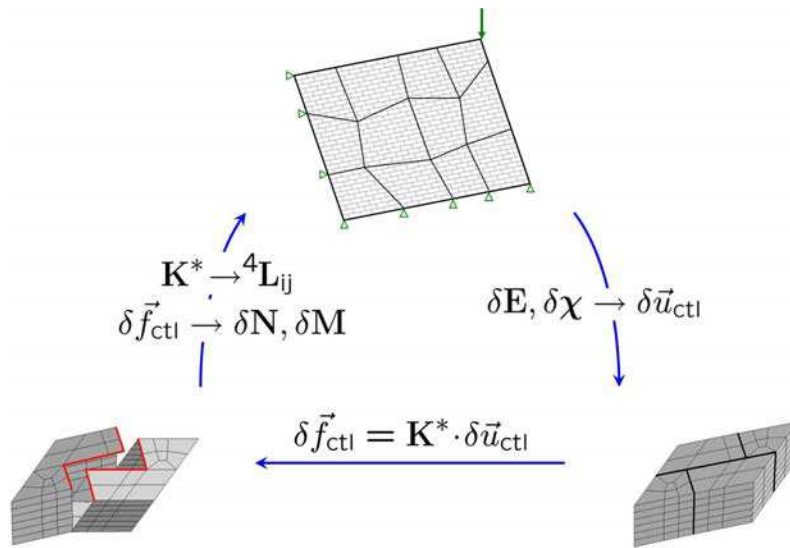


Fig. 12.  $FE^2$  computational scheme for shell structures.

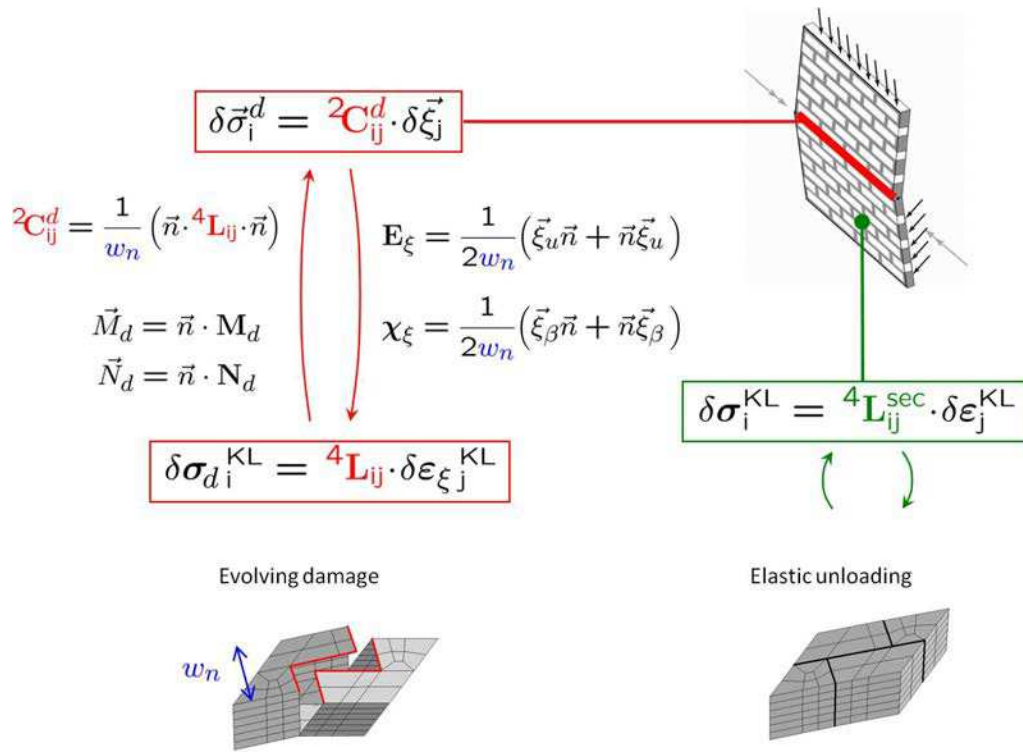


Fig. 13. Localisation-enhanced  $FE^2$  computational scheme for shell structures.

stress tensors, tangent stiffnesses) to corresponding discontinuity variables were recently developed in [34] based on an energy equivalence argument. These relations are illustrated in Fig. 13. The identified macroscopic equivalent responses of the bulk of the shell and of the discontinuity are casted in a thin shell format (Kirchhoff-Love assumption). As a result, the scale transition does not furnish the information related to the shear behaviour. A Mindlin planar shell formulation is however used at the structural scale (DST – Discrete Shear Triangle), which requires a specific treatment of transverse shear both for its interpolation (to avoid shear locking) and for the related material behaviour. For full details concerning these aspects, the reader is referred to [34].

## 5.2. Anisotropic flexural response of masonry wallets

The proposed localisation enhanced  $FE^2$  framework is used here to analyse the structural response of a masonry panel loaded perpendicular to its plane as illustrated in Fig. 14. The structure consists in a three point bending test on a panel which is supported on its two shortest sides. The orientation of the masonry material symmetry axes is chosen in a non-standard way such that the stair-case crack orientation is aligned with the supported sides. The wall size is 1200 mm  $\times$  600 mm with a thickness of 53 mm, while the unit cell dimensions are chosen as  $l = 88$  mm with  $d = h = 44$  mm. The

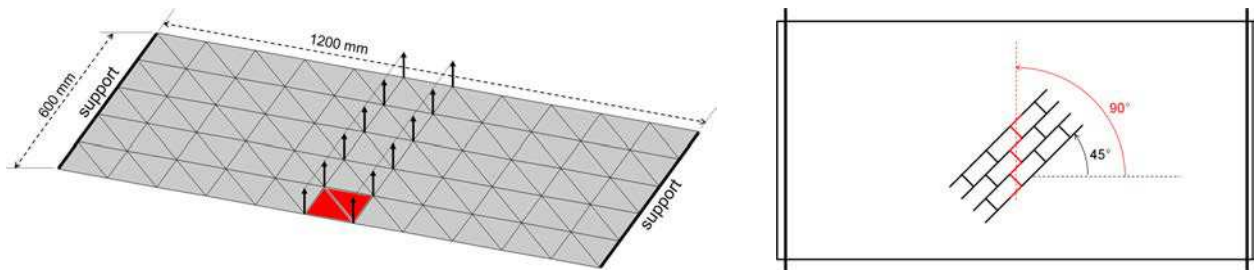
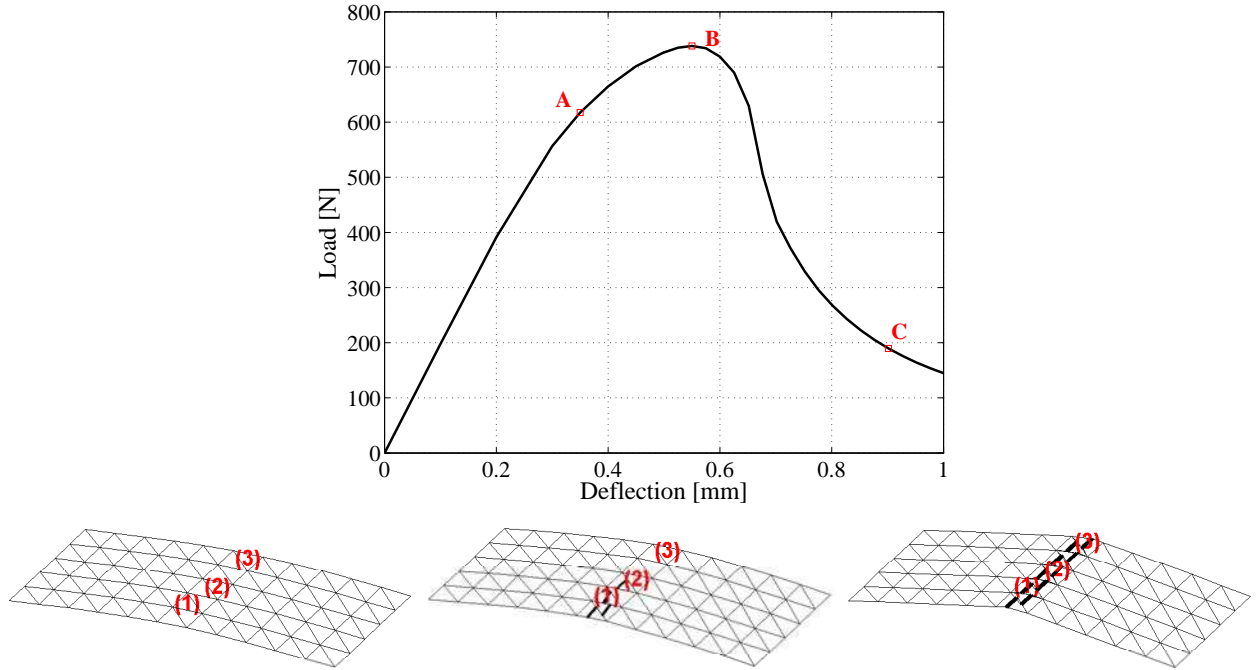


Fig. 14. Problem set-up for the masonry wallet structural computation. Structural finite element discretisation with imperfection (in red – left), (right) orientation of joints with respect to the overall structure.

material parameters used at the fine scale considered in this computation are reported in Table 3. These values correspond to a fine-scale description in which only the Mohr-Coulomb failure criterion is active. In order to show the ability of the framework to properly describe crack propagation, an initial imperfection is assumed in the wallet in a zone corresponding to two elements. In this imperfect zone, the tensile strength, the cohesion and the fracture energy of joints are all decreased by a factor 2. The results of the test are depicted in Figs. 15 to 17. As depicted in Fig. 15, the response of the structure can be traced until far in the post-peak regime (the computation is performed under displacement control). Cracking initiates in the weakened zone. The peak load

**Table 3.** Material parameters for FE<sup>2</sup> computation on masonry wallet: (a) Brick and (b) mortar/mortar-brick interface.

	$E$ [MPa]	$\nu$	$k_n$ [MPa/mm]	$k_t$ [MPa/mm]	$f_t$ [MPa]	$G_f$ [mJ/mm <sup>2</sup> ]	$c$ [MPa]	$\varphi$ [°]	$f_c$ [MPa]	$\vartheta$ [°]
(a)	16700	0.15	—	—	—	—	—	—	—	—
(b)	—	—	438	182	0.38	0.02	0.28	36	$\infty$	80



**Fig. 15.** Structural response of the masonry panel with deformed configuration at different stages of the cracking process.

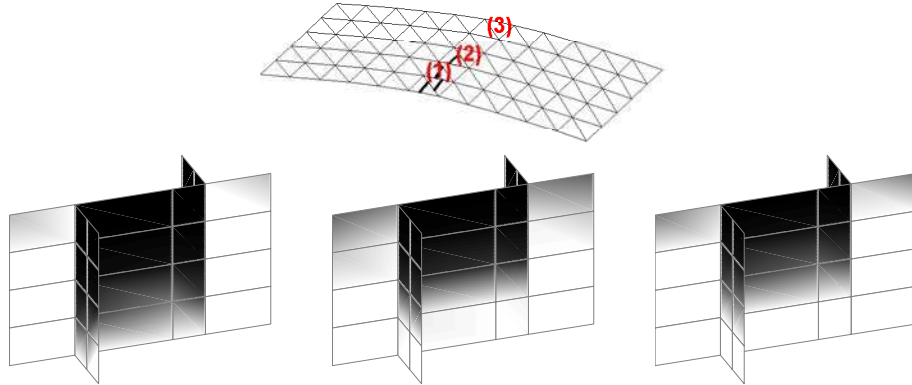


**Fig. 16.** Deformed configuration and damage maps of the masonry panel at stage B.

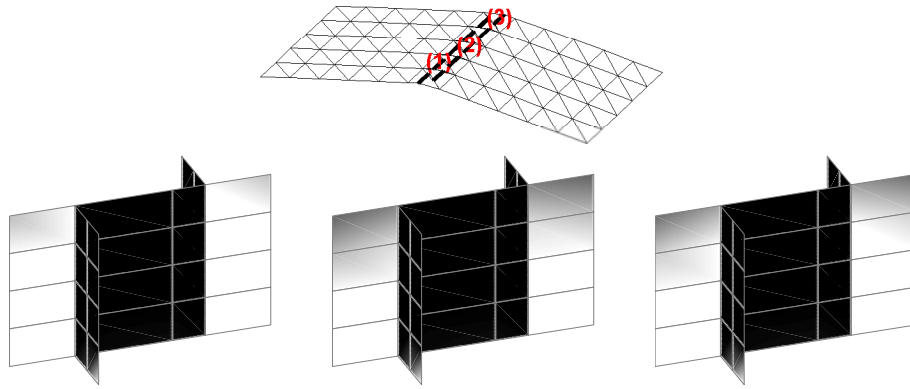


**Fig. 17.** Deformed configuration and damage maps of the masonry panel at stage C.

is obtained when the localising discontinuity propagation reaches half of the structure width. At the peak load, it can be seen in the cell states depicted in Fig. 16 that the flexural stair-case damage pattern is well developed, even in at the position where structural scale localisation is not reached yet (point (3)). The damage pattern is however more developed across the thickness in the first cracking elements (point (1)). Since the crack is not fully propagated to the complete width of the structure, the deformed configuration of the structure at the peak load still exhibits a more or less distributed curvature. On the contrary, at the end of the structural softening tail (point C – Fig. 17), the stair-case crack pattern is fully developed in the unit cells across the complete structure. Figure 17 clearly shows a localised curvature at the structural scale due to the discontinuities, with unloaded portions of the wallet.

## 6. CONCLUSIONS

A shell-oriented computational homogenisation framework was presented and applied to practical situations. Based on a generalisation of periodic homogenisation, scale transitions were presented which allow using through-thickness 3D RVEs to extract the average response of heterogeneous shells with complex microstructures. These scale transitions were applied to two types of materials, showing that flexural effects cannot be neglected in practical applications. First, the effect of bending terms in the homogenisation of textile reinforced composites was assessed by means of RVE computations. The shell homogenisation framework allowed to illustrate the importance of flexural effects on the potential delamination failure mode of single ply conveyor belts. Another example featuring a four ply RVE showed that this effect is even more important in that case. Second, the computational homogenisation framework was used in combination with a macroscopic localisation detection for masonry cracking. The importance of incorporating membrane-flexural couplings in the detection of structural localisation for quasi-brittle materials was underlined by means of an RVE computation example. The incorporation of macroscopic localisation of degradation in  $FE^2$  computational schemes was discussed and illustrated on a masonry wallet computation. Future developments of the presented framework are related to the simulation of delamination in textile reinforced composites.

## ACKNOWLEDGEMENTS

The authors gratefully acknowledge the support of F.R.S.-FNRS for intensive computation facilities. The second and fourth authors are supported as F.R.S.-FNRS post-doctoral researcher. The first and third authors are supported in the frame of a scientific impulsion grant.

## REFERENCES

- [1] S.L. Angioni, M. Meoa, A. Foreman. A comparison of homogenization methods for 2-D woven composites *Composites: Part B*, **42**: 181–189, 2011.
- [2] M. Ansar, W. Xinwei, Z. Chouwei. Modeling strategies of 3D woven composites: A review *Composite Structures*, **93**: 1947–1963, 2011.
- [3] F. Armero and D. Ehrlich. Finite element methods for the multi-scale modeling of softening hinge lines in plates at failure. *Computer Methods in Applied Mechanics and Engineering*, **195**(13–16): 1283–1324, 2006.
- [4] P. Badel, E. Vidal-Salle, E. Maire, and P. Boisse. Simulation and tomography analysis of textile composite reinforcement deformation at the mesoscopic scale. *Composites Science and Technology*, **68**: 2433–2440, 2008.
- [5] T. Belytschko, S. Loehnert, and J.H. Song. Multiscale aggregating discontinuities: A method for circumventing loss of material stability. *International Journal for Numerical Methods in Engineering*, **73**(6): 869–894, 2008.
- [6] T. Belytschko and J.H. Song. Coarse-graining of multiscale crack propagation. *International Journal for Numerical Methods in Engineering*, **81**: 537–563, 2010.
- [7] A. Bensoussan, J.L. Lions, and G. Papanicolaou. *Asymptotic analysis for periodic structures*. North-Holland Publishing Company, 1978.
- [8] J. Besson, G. Cailletaud, J.L. Chaboche and S. Forest *Mécanique non linéaire des matériaux*, Hermès, 2001.
- [9] J. Besson and R. Foerch. Large scale object oriented finite element code design. *Computer Methods in Applied Mechanics and Engineering*, **142**: 165–187, 1997.
- [10] R. de Borst, L.J. Sluys, H.B. Muhlhaus, and J. Pamin. Fundamental issues in finite element analyses of localization of deformation. *Engineering Computations*, **10**(2): 99–121, 1993.
- [11] S. Brasile, R. Casciaro, and G. Formica. Multilevel approach for brick masonry walls – Part I: A numerical strategy for the nonlinear analysis. *Computer Methods in Applied Mechanics and Engineering*, **196**: 4934–4951, 2007.
- [12] P. Cartraud and T. Messenger. Computational homogenization of periodic beam-like structures. *International Journal of Solids and Structures*, **43**(3–4): 686–696, 2006.
- [13] A. Cecchi and K. Sab. A homogenized Reissner-Mindlin model for orthotropic periodic plates: Application to brickwork panels. *International Journal of Solids and Structures*, **44**(18–19): 6055–6079, 2007.
- [14] K.S. Challagulla, A. Georgiades, G.C. Saha, and A.L. Kalamkarov. Micromechanical analysis of grid-reinforced thin composite generally orthotropic shells. *Composites Part B-Engineering*, **39**(4): 627–644, 2008.
- [15] E.W.C. Coenen, V.G. Kouznetsova, and M.G.D. Geers. Computational homogenization for heterogeneous thin sheets. *International Journal for Numerical Methods in Engineering*, **83**(8–9): 1180–1205, 2010.
- [16] S. Daggumati, W. Van Paepegem, J. Degrieck, J. Xu, S.V. Lomov, I. Verpoest. Local damage in a 5-harness satin weave composite under static tension: Part II – Meso-FE modelling. *Composites Science and Technology*, **70**: 1934–1941, 2010.
- [17] V.S. Deshpande, N.A. Fleck. Collapse of truss core sandwich beams in 3-point bending. *International Journal of Solids and Structures*, **38**: 6275–6305, 2001.
- [18] F. Feyel and J.L. Chaboche. FE<sup>2</sup> multiscale approach for modelling the elastoviscoplastic behaviour of long fiber SiC/Ti composite materials. *Computer Methods in Applied Mechanics and Engineering*, **183**(3–4): 309–330, 2000.
- [19] A. Gasser, P. Boisse and S. Hanklar. Mechanical behaviour of dry fabric reinforcements. 3D simulations versus biaxial tests. *Computational Materials Science*. **17**: 7–20, 2000
- [20] M.G.D. Geers, E.W.C. Coenen, and V.G. Kouznetsova. Multi-scale computational homogenization of structured thin sheets. *Modelling and Simulation in Materials Science and Engineering*, **15**(4): S393–S404, 2007.
- [21] A. Ibrahimbegovic and D. Markovic. Strong coupling methods in multi-phase and multi-scale modeling of inelastic behavior of heterogeneous structures. *Computer Methods in Applied Mechanics and Engineering*, **192**(28–30): 3089–3107, 2003.
- [22] D.S. Ivanov, S.V. Lomov, S.G. Ivanov, I. Verpoest. Stress distribution in outer and inner plies of textile laminates and novel boundary conditions for unit cell analysis. *Composites: Part A*, **41**: 571–580, 2010.
- [23] H.E. Johnson, L.A. Louca, S. Mouring, A.S. Fallah. Modelling impact damage in marine composite panels *International Journal of Impact Engineering*, **36**: 25–39, 2009.
- [24] A.L. Kalamkarov, I.V. Andrianov, and V.V. Danishevs’kyy. Asymptotic homogenization of composite materials and structures. *Applied Mechanics Reviews*, **62**(3), 2009. Article Number: 030802.
- [25] V.G. Kouznetsova, W.A.M. Brekelmans, and F.P.T. Baaijens. An approach to micro-macro modeling of heterogeneous materials. *Computational Mechanics*, **27**(1): 37–48, 2001.
- [26] V.G. Kouznetsova, M.G.D. Geers, and W.A.M. Brekelmans. Multi-scale second-order computational homogenization of multi-phase materials: a nested finite element solution strategy. *Computer Methods in Applied Mechanics and Engineering*, **193**(48–51): 5525–5550, 2004.
- [27] J. Lemaitre, J.L. Chaboche *Mécanique des matériaux solides*, Dunod, 1985.
- [28] S.V. Lomov et al. Meso-FE modelling of textile composites : Road map, data flow and algorithms. *Composites Science and Technology*, **67**: 1870–1891, 2007.



- [29] J. Makowski and H. Stumpf. Strain localization in stress-resultant theory of shells. *Mechanics Research Communications*, **25**(4): 455–465, 1998.
- [30] T.J. Massart, R.H.J. Peerlings, and M.G.D. Geers. An enhanced multi-scale approach for masonry wall computations with localization of damage. *International Journal for Numerical Methods in Engineering*, **69**(5): 1022–1059, 2007.
- [31] T.J. Massart, R.H.J. Peerlings, and M.G.D. Geers. Structural damage analysis of masonry walls using computational homogenization. *International Journal of Damage Mechanics*, **16**: 199–226, 2007.
- [32] B.C.N. Mercatoris, P. Bouillard, and T.J. Massart. Multi-scale detection of failure in planar masonry thin shells using computational homogenisation. *Engineering Fracture Mechanics*, **76**(4): 479–499, 2009.
- [33] B.C.N. Mercatoris and T.J. Massart. Assessment of periodic homogenization-based multiscale computational schemes for quasi-brittle structural failure. *International Journal for Multiscale Computational Engineering*, **7**(2): 153–170, 2009.
- [34] B.C.N. Mercatoris and T.J. Massart. A coupled two-scale computational scheme for the failure of periodic quasi-brittle thin planar shells and its application to masonry. *International Journal For Numerical Methods in Engineering*, **85**: 1177–1206, 2011.
- [35] M. Mistler, A. Anthoine, and C. Butenweg. In-plane and out-of-plane homogenisation of masonry. *Computers & Structures*, **85**(17–18): 1321–1330, 2007.
- [36] G. Nilakantan, M. Keefe, T.A. Bogetti, R. Adkinson, J.W. Gillespie. On the finite element analysis of woven fabric impact using multiscale modeling techniques. *International Journal of Solids and Structures*, **47**: 2300–2315, 2010.
- [37] R.H.J. Peerlings and N.A. Fleck. Computational evaluation of strain gradient elasticity constants. *International Journal for Multiscale Computational Engineering*, **2**(4): 599–619, 2004.
- [38] B. Piezel. Comportement et analyse multi-échelles d’un composite à renfort tissé tridimensionnel. *PhD Thesis*, Mines ParisTech, France, 2010.
- [39] B. Piezel, L. Laiarinandrasana, E. Mansour, J. Renard, and A. Thionnet. Analyse expérimentale d’un composite textile en vue d’une modélisation multi-échelles. *16e Journées Nationale sur les Composites – JNC 16*, France, 2009.
- [40] R.J.M. Smit, W.A.M. Brekelmans, and H.E.H. Meijer. Prediction of the mechanical behavior of nonlinear heterogeneous systems by multi-level finite element modeling. *Computer Methods in Applied Mechanics and Engineering*, **155**(1–2): 181–192, 1998.
- [41] P. Suquet. *Elements of homogenization for inelastic solid mechanics*. In: *Homogenization techniques for composite media.*, volume 272. Springer-Verlag, Berlin, 1987.
- [42] K.I. Tserpes, G. Labeas, S. Pantelakis. Multi-scale modeling of the mechanical response of plain weave composites and cellular solids. *Theoretical and Applied Fracture Mechanics*, **54**: 172–179, 2010.
- [43] I. Verpoest and S.V. Lomov. Virtual textile composites software *WiseTex*: Integration with micro-mechanical, permeability and structural analysis. *Composites Science and Technology*, **65**: 2563–2574, 2005.
- [44] P.N. Vinh, O. Lloberas-Valls, M. Stroeve, L.J. Sluys. Homogenization-based multiscale crack modelling: From micro-diffusive damage to macro-cracks. *Computer Methods in Applied Mechanics and Engineering*, **200**(9–12): 1220–1236, 2011.
- [45] H.N.G. Wadley, N.A. Fleck, A.G. Evans. Fabrication and structural performance of periodic cellular metal sandwich structures. *Composites Science and Technology*, **63**: 2331–2343, 2003.
- [46] J. Zeman and M. Šejnoha. From random microstructures to representative volume elements. *Modelling and Simulation in Materials Science and Engineering*, **15**(4): S325–S335, 2007.